



A Performance Analysis of an Electric Two Stage Supersonic Propeller

Jens Kunze! Allan Paull2

Abstract

An aerodynamic and thermodynamic analysis of a supersonic propeller driven by an electric motor is performed. In this analysis, three different configurations, i.e. single-rotor, rotor-stator and double-rotor, are investigated using a quasi 3D model. For a meaningful comparison between configurations, trim drag, caused by balancing the net torque of the propeller, has to be considered. The models used in a previous study are, therefore, extended to be able to estimate trim drag as well as calculating the flow condition between propeller stages. It is shown that two counter rotating propellers can offer significant performance benefits over single-stage systems by reducing or entirely removing the need for trimming about the roll axis. Rotor-stator configurations, on the other hand, are less efficient than single-rotor configurations at peak efficiency, but outperform them at high motor speeds. They, thus, can provide the best solution for specific scenarios but are not universally better than single-rotor systems and always less efficient than double-rotor configurations. Finally, a CFD analysis of two counter rotating stages is performed and compared to the quasi 3D results. Good agreement is found between the two methods, both in overall quantities, like the power efficiency and thrust power of the blade, as well as local flow properties.

Keywords: Electric Propulsion, Supersonic Propeller

1. Introduction

The recent improvements in battery technology, sparked to a large extent by the electric car industry [1], have caused many industries to consider transitioning away from combustion engines to electric systems [2]. Contemporary batteries offer higher specific energy and higher specific power, i.e. energy and power per unit mass, and higher energy density and higher power density, i.e. energy and power per unit volume, as well as increased reliability and longer life cycles. Electric motors, too, have become smaller, lighter and more powerful. These developments are projected to continue into the foreseeable future, [3].

Even electric propulsion of aircraft and spacecraft has been possible for several years. A variety of methods exists for the propulsion of small satellites and other spacecraft [4]. Drones and other small remote controlled aircraft have surpassed the stage of a mere hobby and have found applications in several industries [5]. Electric motors can much more readily be scaled down so that aircraft of almost any size are now being studied [6] and entirely new configurations are imaginable. Power electronics on aircraft are beginning to replace the traditional hydraulic systems [7]. Indeed, even small low-speed short distance electric passenger aircraft are already a reality [8] and research is ongoing to electrify large civil aircraft, too [9]. However, to the authors' knowledge, high-speed and supersonic flight have not been realised to date. The most likely reason are the aforementioned specific power and specific energy of electric energy storage systems (EESS). Typical specific power over the specific energy of different EESS are shown in Fig. 1. In general, there appears to exist a trade-off between specific energy and specific power and no EESS excels in both at the same time. The most promising candidates for electric flight are Li-ion batteries and supercapacitors.

¹Centre for Hypersonics, School of Mechanical and Mining Engineering, The University of Queensland, 4072 Brisbane, j.kunze@uq.edu.au

²Centre for Hypersonics, School of Mechanical and Mining Engineering, The University of Queensland, 4072 Brisbane, allan.paull@uq.edu.au

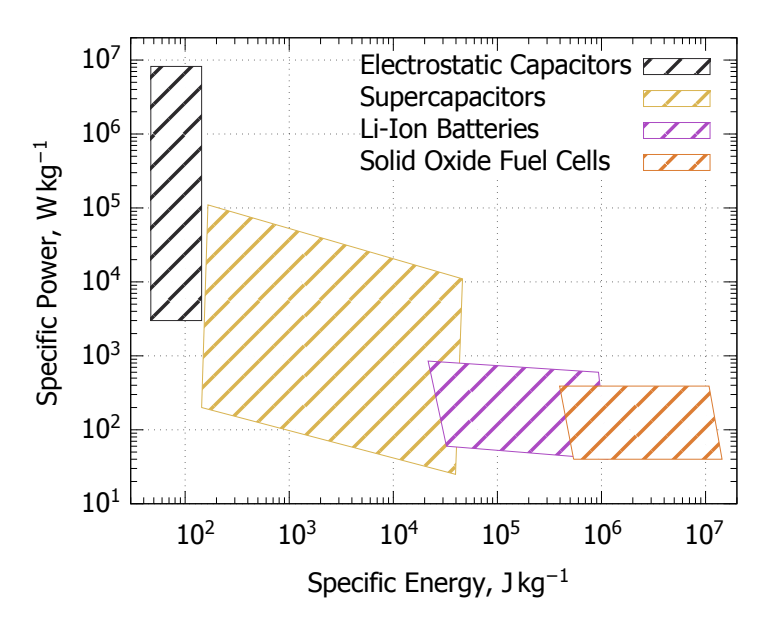


Fig 1. Typical specific power over specific energy for different electric energy storage systems, reproduced from [10].

Contemporary batteries, however, are not yet able to compete with combustion based systems; commonly cited values for the specific energy of state-of-the-art lithium-ion batteries are around 1 MJ/kg compared to 43 MJ/kg for jet fuels. Considering specific power on the other hand, it was recently shown in an experimental analysis of batteries intended for remote controlled aircraft [11] that approximately 300 A, or 7 kW/kg, can be achieved for around 30 s. Supercapacitors can reach even higher values [10, 12].

In a previous study [13], it was shown that modern EESS are already capable of powering small vehicles for short flights at supersonic speeds. It was, furthermore, demonstrated that, based on two dimensional analysis, an electric supersonic propeller is feasible from an aerodynamic and thermodynamic point of view. In this study, the analysis is extended to incorporate two stage propeller configurations. There are two strong arguments in favour of using two stages as opposed to one, as has been demonstrated for subsonic propellers [14]. The first is that a second stage can recuperate some of the angular momentum introduced to the flow by the first stage and, thus, improve the overall efficiency. And secondly, a second stage can counteract the torque of the first stage and, thereby, reduce or completely remove the need to trim the vehicle against roll. Figure 2 shows a schematic of a two stage propeller configuration with reference station numbering. In the following, different propeller configurations will be analysed using

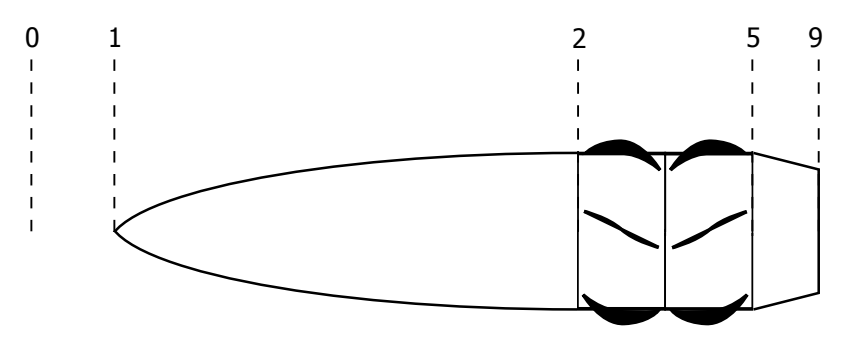


Fig 2. A schematic of a two stage propeller vehicle with station numbering.

a quasi 3D adaptation of the analytical 2D model presented by Kunze and Paull [13]. Two types of two stage configurations will be investigated in detail; a rotor-stator configuration (RSC) and a double-rotor configuration (DRC). These will be compared to single-rotor configurations (SRC). Trim drag is calculated for each configuration to allow for a meaningful comparison. Finally, a CFD analysis of two counter rotating propeller stages is performed and compared to the analytical model.

2. Modelling

The majority of the aerodynamic and thermodynamic models used here are as described in [13]. The inviscid flow properties are calculated using the shock-expansion method [15], where the air is treated as a perfect gas with $\gamma=1.4$. Viscous forces are calculated with the reference enthalpy method [16]. Wall temperatures are calculated by treating the blade as a radiation adiabatic wall [17], where empirical correlations are used to find the required boundary layer thicknesses [17, Appendix B, pp.337-350]. Since the air temperature near the wall can exceed 1000 K the specific heats, thermal conductivity and viscosity are treated as temperature dependant. The properties are calculated assuming chemical equilibrium for air with the following composition: 78.1 % N₂, 20.9 % O₂, 0.94 % Ar and 0.032 % CO₂ by volume [18, pp.19-21]. The required material constants can be found in [19].

However, in this study the 2D model is modified to be quasi 3D. That is to say that, instead of only calculating the flow conditions on the centre line of the blade and assuming they are constant with radius, the blades are now split into 10 cross-sections. Each cross-section has the same height, i.e. a 30 mm tall blade consists of 10 3 mm tall cross-sections, and is treated as a 2D blade. This accounts for the dependence of rotational velocity on the distance to the axis of rotation. It, furthermore, allows for more complex blade geometries since the chord length of each cross-section can be defined individually. In addition to rectangular blade planforms, trapezoidal and triangular planforms are now possible. The flow on each cross-section is uniform and there is no interaction between cross-sections, hence, there is no cross flow and tip effects are ignored. In order to determine how many cross-sections to use, a convergence study was performed. The model was used to calculate the power efficiency of 30 mm tall blades with 2, 5, 10, 20, 40 and 80 cross-sections at motor speeds of 40 min⁻¹ to 85 min⁻¹. In Fig 3 the results of the convergence study for the quasi 3D model are shown. Figure 3a shows the maximum

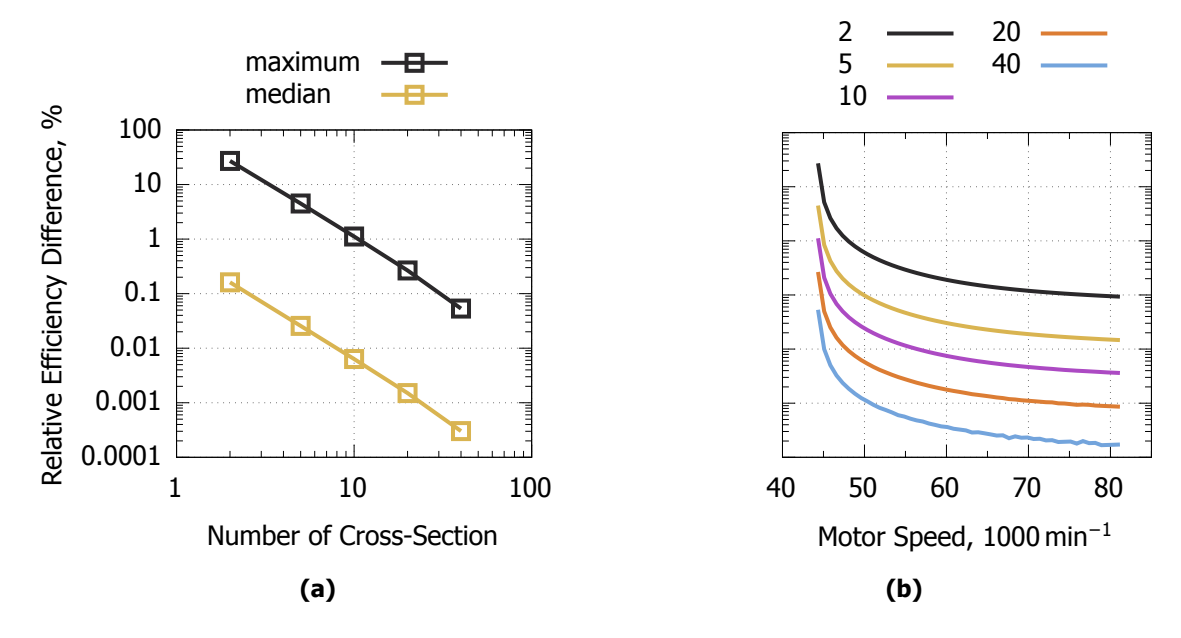


Fig 3. The convergence metrics for the quasi 3D model.

relative difference in power efficiency over the number of cross-sections relative to the quasi 3D blade with 80 cross-sections as well as the median relative difference. In Fig. 3b the relative difference in

power efficiency over the motor speed is shown for each case. It was found that 3 mm tall cross-sections, i.e. 10 cross-sections in total, provide sufficient resolution to adequately capture the change in blade speed with radius.

The extension to two stage systems requires additional assumptions and modelling, which are described in the following. In order to make a useful comparison between two stage and single stage systems, a vehicle level consideration, namely trimming about the roll axis, has to be included. The propulsion efficiency can be significantly affected by the associated trim drag. Since both DRCs and RSCs effectively reduce the net torque applied to the vehicle they are inherently more stable than SRCs and, thus, require smaller forces to trim the vehicle. To account for this, a simple trim drag model is included in this study.

The second model introduced here is the calculation of the flow conditions between the two propeller stages. The two dimensional flow model described in [13] is not equipped to handle non-uniform flows. It is, thus, necessary to convert the complex flow behind the first stage into an approximately equivalent and uniform flow. Control volume analysis is used here to achieve this.

2.1. Trim Drag Calculation

The aim of trimming the vehicle about the roll axis is to counteract any moments about this axis, i.e.

$$\sum_{i} M_i + M_{tr} = 0, \tag{1}$$

where M_i designates the torque of propeller stage i and M_{tr} designates the trimming torque. Control surfaces are used for this purpose. They are generally placed such that the moment arm with respect to the axis of rotation is large so the control surfaces themselves and the required deflection angles can be kept small. Deflecting a control surface creates both the moment required to balance the vehicle and additional drag as a function of its deflection angle and surface area.

It is assumed here that the wingspan of the vehicle is 1 m. Two rectangular control surfaces of $100 \, \text{mm} \times 50 \, \text{mm}$ with a lever arm of $450 \, \text{mm}$ with respect to the propeller axis are used. The trim torque and drag can be calculated from the pressure difference over the control surface, the control surface area and the deflection angle:

$$M_{tr} = 2 \cdot \cos(\theta_{cs}) A_{cs} \Delta p_{cs} l_{cs}$$
 and (2)

$$F_{tr} = 2 \cdot \sin(\theta_{cs}) A_{cs} \Delta p_{cs}. \tag{3}$$

Here, θ_{cs} is the control surface deflection angle, A_{cs} the surface area of each control surface, Δp_{cs} is the static pressure difference across the control surface and l_{cs} is the control surface lever. The required θ_{cs} is calculated using shock expansion theory and assuming zero thickness with a shock on one side of the control surface and an expansion on the other. For simplicity, it is assumed that the control surfaces are exposed to the freestream.

2.2. Two Stage Modelling

Figure 4 shows a schematic of two propeller blades and the associated velocity vectors. Here, $\vec{u}_{20} = \vec{u}_{21}$, $\vec{c}_{21} = \vec{c}_{22}$ and $\vec{u}_{22} = \vec{u}_{5}$. Figure 5 shows the control volume drawn between two flat plate blades. It should be noted that the approach is valid for arbitrary blade shapes as there is no flow through the blades and, thus, the shape of the control volume on the sides is irrelevant. The external forces are known from the calculation of the first stage, see [13]. Alternatively, the control volume can be drawn as a hollow cylinder around the entire first stage. The equations for the given case are:

continuity:
$$\dot{m}_z = \rho_{20} w_{z20} A_{20} = \rho_{21} w_{z21} A_{21},$$
 (4)

z-momentum:
$$p_{20}A_{20} + F_T - p_{21}A_{21} = \dot{m}_z \left(w_{z21} - w_{z20} \right),$$
 (5)

y-momentum:
$$F_D = \dot{m}_z \left(w_{y21} - w_{y20} \right) \qquad \text{and} \qquad \qquad \textbf{(6)}$$

energy:
$$\dot{Q} - \dot{W} = \dot{m}_z \left(\frac{\left| \vec{w}_{21} \right|^2 - \left| \vec{w}_{20} \right|^2}{2} + c_p \left(T_{21} - T_{20} \right) \right). \tag{7}$$

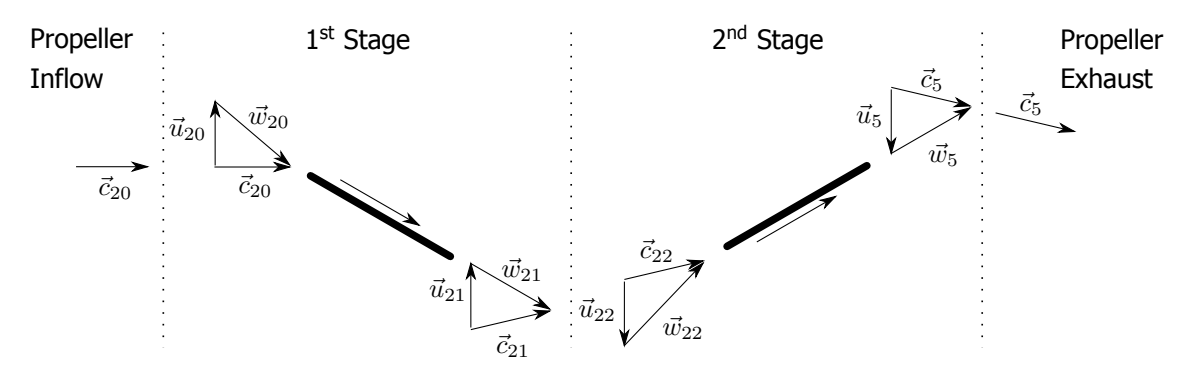


Fig 4. A schematic of a two stage propeller with global and relative velocity vectors.

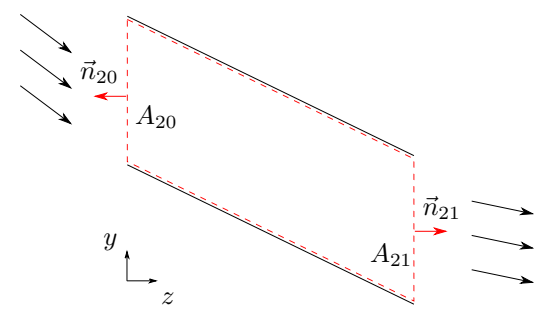


Fig 5. The control volume between two blades of the first stage used to calculate the uniform inflow conditions for the second stage.

 F_T designates the blade thrust and F_D the blade drag. \dot{Q} is the heat flow to the fluid and \dot{W} is the shaft work, which, by convention, is negative if the work is done by the shaft on the fluid. Additionally, the blade relative velocity vector is given by

$$\vec{w} = \begin{pmatrix} 0 \\ w_y \\ w_z \end{pmatrix} \tag{8}$$

and

$$A_{20} = A_{21} = \frac{2\pi}{n_b} \left(r_h + \frac{h_b}{2} \right), \tag{9}$$

where n_b denotes the number of blades on the stage, r_h indicates the hub radius and h_b designates the blade height. With the above equations the uniform inflow conditions for the second stage can be calculated and the methods presented in [13] can be applied to calculate the properties of the second stage.

In reality, the inflow for the second stage is a complex and highly unsteady flow consisting of high pressure and low pressure regions. For small numbers of blades it is expected that there will also be regions of undisturbed freestream in the second stage inflow. These phenomena can not be accounted for with the presented model.

2.3. Computational Modelling

The computational analysis in this study was performed using Eilmer4 [20]. Eilmer4 is the Centre for Hypersonic's in-house finite-volume flow solver, specifically designed for high-speed flow conditions. It, furthermore, provides a rotating frame of reference, which can be used to design and analyse turbo-machinery [21]. All simulations presented in the following were performed using a rotating frame of reference.

Two counter rotating propeller stages were simulated separately. Each simulation calculates the conditions of a single blade. Either side of the blade is a periodic boundary condition, halfway to where the adjacent blade would be. The surfaces of the blade and the propeller hub are modelled as adiabatic walls without slip. At the outflow boundary, the flow properties are simply extrapolated from the last cells. For the inflow conditions, an axisymmetric simulation of a power law forebody flying at Mach 4 and 15 km was performed first. The forebody contour is described by

$$r = r_h \left(\frac{z}{l_{fb}}\right)^{0.7},\tag{10}$$

where $l_{fb}=8r_h$ is the total length of the forebody. The flow profile at the corner of the forebody was then used as the inflow condition for the first stage. Figure 6 shows the flow conditions as a function of radius. The pressure is approximately constant, however, in both the temperature and the velocity

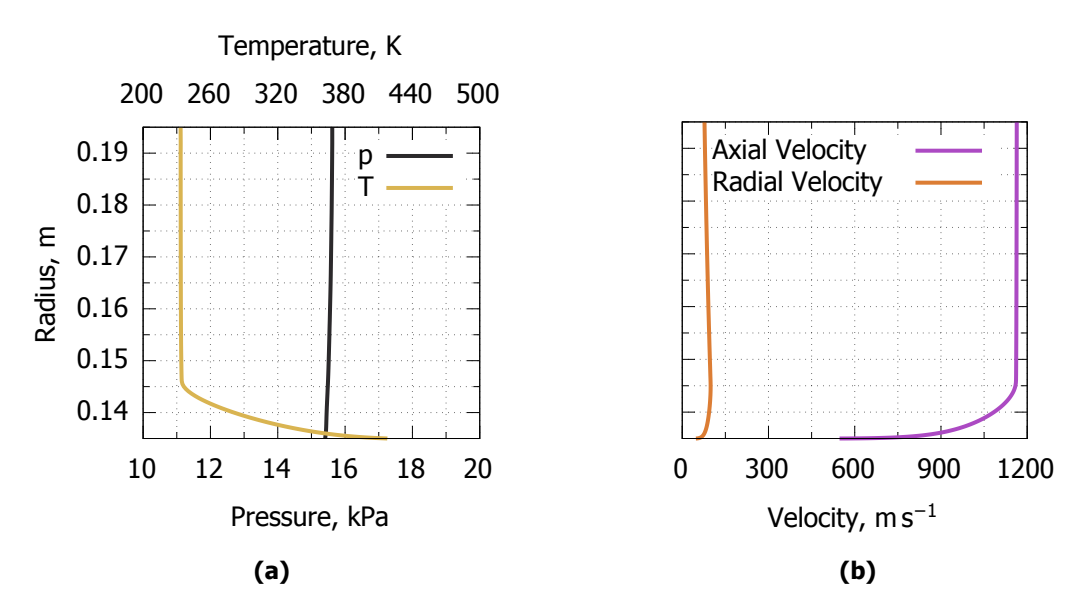


Fig 6. The inflow conditions for the first stage simulation.

profiles an approximately 10 mm thick boundary layer can be seen.

For the simulation of the second stage, the flow conditions downstream of the first stage are used as the inflow condition. The flow properties 6.7 mm downstream of the first stage are extracted and transferred into the rotating frame of the second stage. In reality, the inflow to the second stage is unsteady and rotating in the opposite direction of the second stage itself. However, in this study, the inflow to the second stage is steady. In order to get a result that more closely resembles reality, the inflow conditions are rotated in increments of 15° around the z-axis and the simulation of the second stage is repeated. This way, the wake of the first stage affects the second stage differently in every simulation. All integrated quantities can then be calculated as the mean of the individual simulations.

The same grid and blade geometry are used used for both stages in this study. However, since the two stages are rotating in opposite directions, the chord angle of the two blades is equal in magnitude but in opposite directions. The grid is structured and contains 673896 cells. Clustering is applied, such that the grid is well resolved around the edges of the blade and the surfaces of the blade and propeller hub. The cell height immediately adjacent to all surfaces is $10\,\mu m$. Twenty four cells resolve the circumference of the blade edges and tip. Considering the edge radius of $0.05\,m m$, the resolution on the edges is as low as $2.08\,\mu m$ per cell. The blade is surounded by an o-grid, such that the cell close to the blade surface are approximately parallel to the blade. The grid of the second stage is shown in Fig. 7.

A grid convergence study was carried out on the first stage only, spinning at 53 000 rotations per

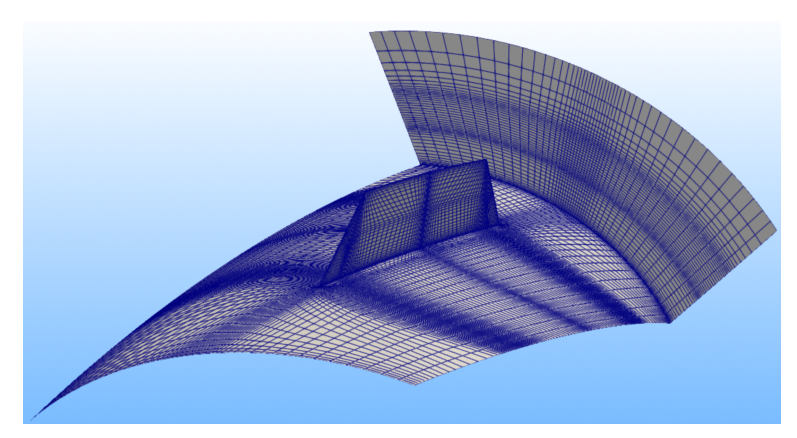


Fig 7. The computational grid of the second stage.

minute. Three different grids were used, with 89 568, 673 896 and 5 391 168 cells respectively. The cell size approximately halves in all three dimensions between each level of grid refinement. In Fig. 8 the results of the grid convergence study and the convergence with the number of steps of a single simulation are shown. Due to the small magnitude in change between all three grid levels, either grid

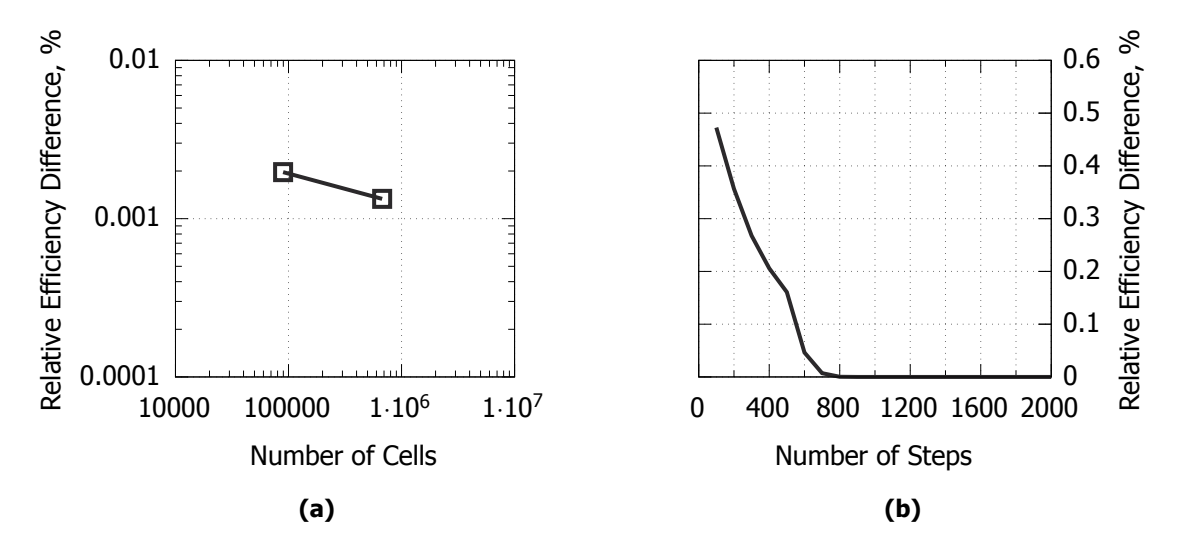


Fig 8. The change in power efficiency with number of cells and number of steps.

would be acceptable for this study. However, considering the difference in conditions between different speeds of rotation and the first and the second stage, the medium grid was chosen.

3. Propeller Analysis

In the following, performance analyses of RSCs, DRCs and trimmed SRCs are presented. Figure 9 shows a rendering of the propeller analysed in this study. In Fig. 10 a drawing of a single propeller blade is shown with the major dimensions indicated. The blade is shown in a 'flattened' coordinate frame, i.e. the cylindrical coordinates r, φ and z, where z is the axis of rotation, are transformed into a cartesian frame where the axes are $r, \varphi r$ and z. Defining the blade in that coordinate frame allows for a more intuitive design process. The subsequent bending around the cylindrical hub is a trivial mathematical operation. The blade and propeller hub dimensions as well as flight conditions, used in this study are shown in table 1. The angle φ indicates the half wedge angle of the blade root cross-section. In the cartesian frame, the blade is symmetrical about two planes, hence φ and γ apply both at the leading

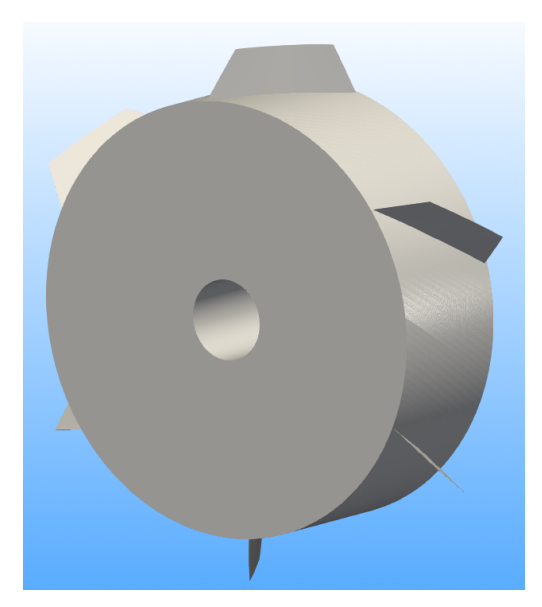


Fig 9. A rendering of the propeller analysed in this study.

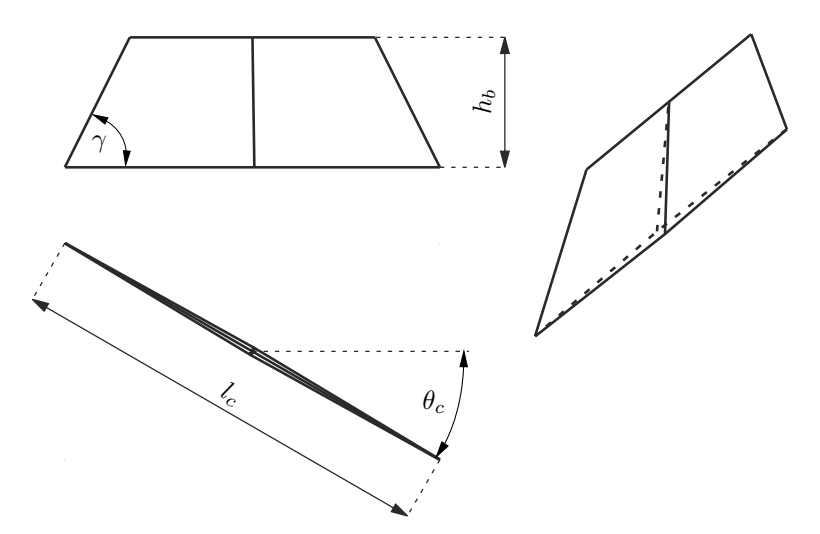


Fig 10. A drawing of a single propeller blade.

Table 1. The blade and hub dimensions and flight conditions.

l_c , mm	h_b , mm	$ heta_{c}$, $^{\circ}$	ϕ , $^{\circ}$	γ , $^{\circ}$	r_h , mm	n_b	Altitude, km	Mach Number
100	30	30	1	60	135	6	15	4

and the trailing edge.

3.1. Single-Rotor Configurations with Trim Drag

In this section, some of the analysis presented in [13, Section 3] is repeated with the added trim drag model. Figure 11 shows the effects of trimming on the efficiency and power output of a single stage propeller. There is a very clear reduction in power output and, as a consequence, the efficiency of the propeller. The effect is larger the higher the velocity ratio, which is understandable since the propeller torque increases with the velocity ratio. Hence, not only is peak efficiency reduced, but the peak is

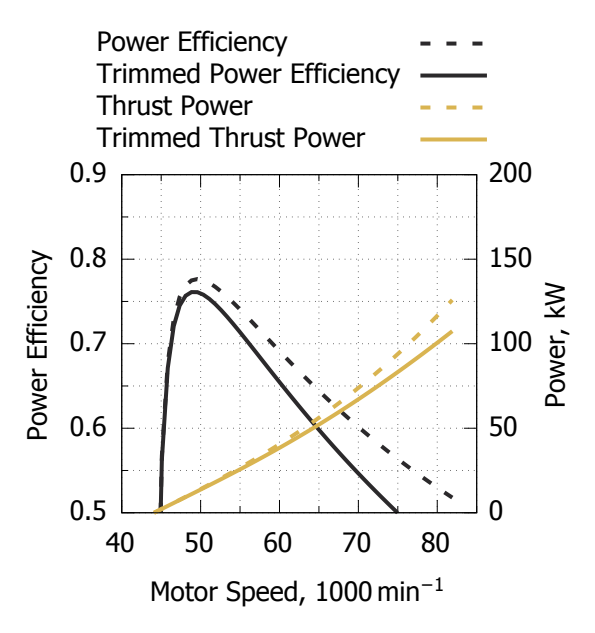


Fig 11. The efficiency and thrust power output of an SRC.

narrower, too. In other words, the propeller's performance becomes more sensitive to small changes in rotational speed or flight conditions.

Figure 12b shows the effect of trimming on the relationship between the blade's chord length and the power efficiency. In [13] it was shown that due to the non-linear nature of viscous drag the efficiency of

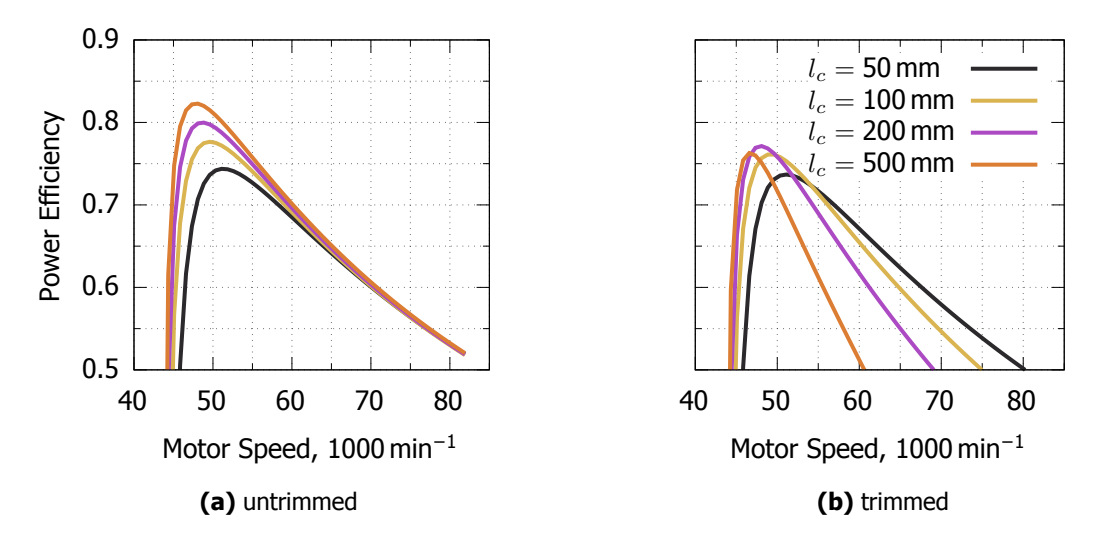


Fig 12. The effects of varying l_c on the power efficiency of an untrimmed and a trimmed SRC.

a blade increases with its length. Factoring in trim drag changes this assertion to an extent, as Fig. 12 shows. When trim drag is considered, the highest peak efficiency of the blades shown in Fig. 12b falls to the blade with $l_c=200\,\mathrm{mm}$. Note, that, although not shown here, blades with $200\,\mathrm{mm} < l_c < 500\,\mathrm{mm}$ can have higher power efficiency peaks than the blades shown. However, in contrast to the untrimmed blades, there is a limit for l_c beyond which the efficiency of the blade decreases. It is, furthermore, evident that the increase in trim drag with increasing velocity ratio is higher for a longer blade, the

longest blade, hence, has the lowest efficiency at higher motor speeds and, thus, the smallest useful range of operation.

3.2. Rotor-Stator Configurations

An RSC consists of a rotating first stage and a non-rotating second stage with either a fixed or a variable chord angle. The ability to vary the chord angle can increase the efficiency of the configuration but comes at a cost of increased overall mass and losses associated with the required mechanism. The data shown in the following is generally applicable to either a fixed or a variable second stage chord angle but does not account for the aforementioned losses.

To evaluate the efficiency of the RSC, the motor speed of the first stage and the chord angle of the second stage are varied within their respective boundaries, and forces, thrust power and motor torque and the power efficiency are calculated for each possible combination. The motor speed is limited at the lower end by the minimum rotational speed to produce any thrust, i.e.

$$\frac{u_{20}}{c_{20}}\Big|_{\min} = \tan^{-1}(\theta_{c,r}),$$
 (11)

where $\theta_{c,r}$ is the chord angle of the rotor. The upper limit is determined by the temperature range of the gas model, i.e. 60 K < T < 5000 K. The chord angle of the stator is varied from $\theta_{c,s} = 0$ to the angle of the flow behind the first stage, i.e.

$$0 \le \theta_{c,s} \le \tan^{-1}\left(\frac{c_{y21}}{c_{z21}}\right),\tag{12}$$

since a stator can only produce thrust in that range. Note, that the angular range increases with the motor speed of the first stage.

In Fig. 13 the efficiency of an RSC using the blade defined in table 1 is shown over the motor speed of the first stage and the chord angle of the stator. Figure 13a shows the power efficiency without factoring in trimming, whereas Fig. 13b includes the effects of trim drag.

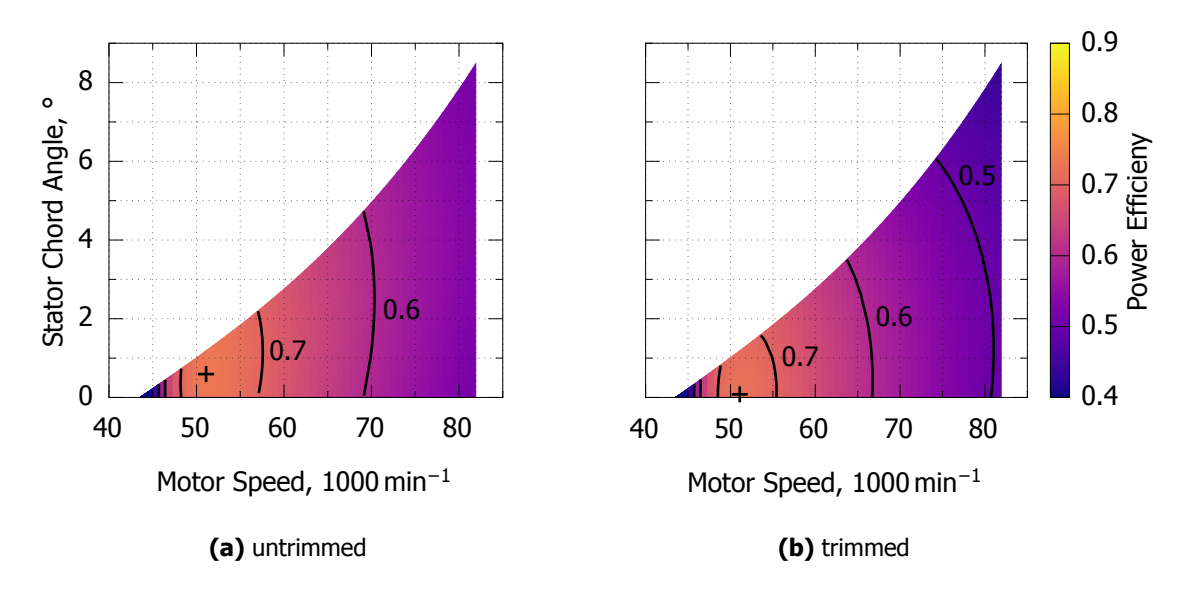


Fig 13. The power efficiency of an RSC.

The most notable observations from Fig. 13a are that:

- 1. for the untrimmed case, the efficiency gradient with respect to the chord angle appears to be quite small indicating that the thrust contributed by the stator is small and
- 2. the efficiency maximum of 0.73 is below that of the trimmed SRC shown in Fig. 11.

In Fig. 13 the power efficiency of the previously discussed SRC, is shown in comparison with the power efficiency at the optimal stator angle of the trimmed and untrimmed RSC. It is clear that, even at optimal

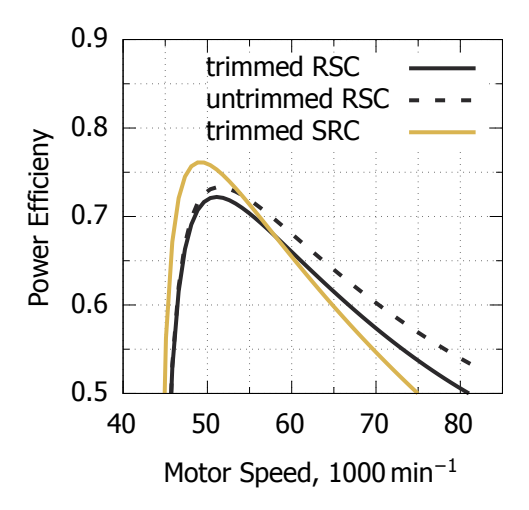


Fig 14. The power efficiency of the trimmed first stage compared to that of the complete RSC at optimal $\theta_{c,s}$ over the motor speed.

stator angles, the RSC only outperforms the SRC for motor speeds above $60\,000\,\mathrm{min^{-1}}$. The trim drag, furthermore, is never completely removed by the stator as the comparison with the untrimmed RSC shows.

The efficiency contribution of the stator over $\theta_{c,s}$ at constant motor speeds, factoring in the reduction in trim drag as well is the thrust it produces, is plotted in Fig. 15a. Figure 15b shows the contribution of the stator to the gross thrust of the RSC. It can be seen that the net effect of the stator is only positive at motor speeds above 60 000 min⁻¹ and peaks at small $\theta_{c,s}$, around 10 % of the maximum. This implies that the main contribution of the stator is not the conversion of angular momentum into thrust, but a reduction of the net torque on the vehicle and, thus, trim drag. Indeed, this is confirmed in Fig. 15b, which shows that stator thrust is highest around 50 % of the maximimal chord angle.

The negative contribution of the stator at lower motor speeds can be attributed to the fact that the flow deflection is so small that the angular momentum added to the flow by the first stage is small as well. Consequentially, realigning the flow with the direction of travel does not yield significant thrust. At higher rotational speeds the angular momentum increases because the flow deflection increases. Using control volume analysis, where the entire first propeller stage is treated as a black box, the conservation of angular momentum yields

$$T_M = \left(r_h + \frac{h_b}{2}\right) c_{\varphi 21} \dot{m}_z,\tag{13}$$

where T_M is the motor torque and $c_{\varphi 21}$ designates the circumferential velocity behind the first stage. For a significant contribution of the stator, there has to be significant angular momentum introduced to the flow by the first stage. The simplest way to achieve that is to increase the motor speed and, therefore, its torque. However, there are practical limits to both motor speed and torque and the power efficiency of the complete RSC decreases with increasing motor speed. Using Equation (13) and assuming that the torque constant, we can assert that reducing r_h will cause \dot{m}_z to decrease and $c_{\varphi 21}$ to increase. Alternatively, at higher altitudes the optimal angle of attack of the first stage increases and, therefore, the angular velocity behind the first stage. However, the main caveat of a stator is that it requires large

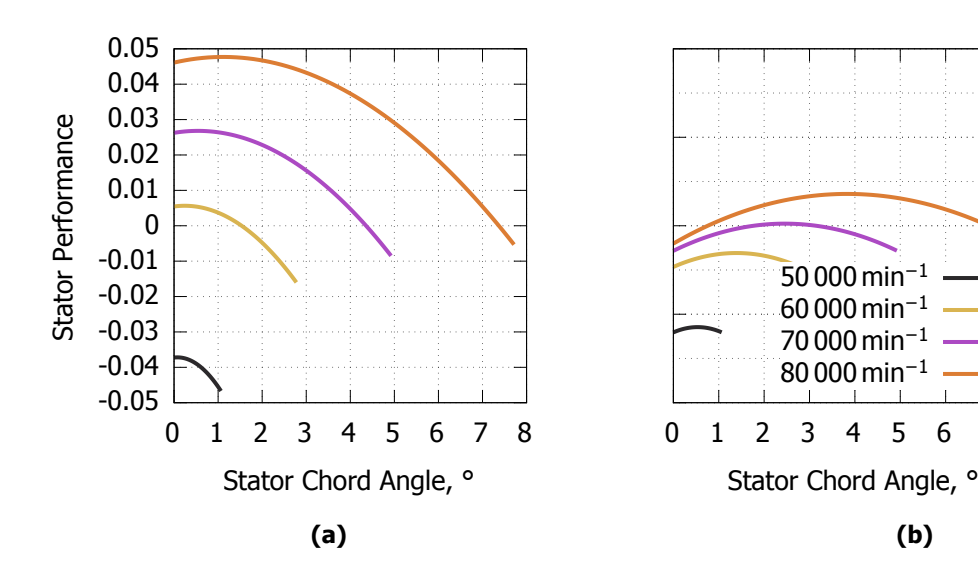


Fig 15. The performance of the stator and its contribution to gross thrust over its chord angle at different motor speeds.

angular momentum behind the first stage to be effective. This implies that the stator is more efficient the less efficient the first stage is. Nevertheless, stators can improve the performance of a vehicle over an SRC under certain conditions and there are likely vehicles for which a stator is beneficial and the best option out of the three configurations studied here.

3.3. Double-Rotor Configurations

A DRC consists of two rotating propeller stages spinning in opposite directions with blades both blades at a fixed chord angle. The rotational speed of either stage can be independently controlled. This means two controllers and motors are needed, however, the power requirement for each individual motor is reduced. With the ability to control both stages the vehicle can be trimmed by the motors without the need to engage flaps. Indeed, they even can be used to manoeuver the vehicle.

To evaluate DRCs the motor speed of both stages is varied. The combined efficiency of both stages is calculated at each combination of rotational speeds. The lower limit for each motor is calculated with equation 11 and the upper limit is again determined by the temperature range of the gas model.

In Fig. 16 two plots on the power efficiency of a DRC over the rotational speeds of both stages are shown. Figure 16a shows the power efficiency of the configuration with contour lines. Figure 16b shows the same plot while including trim drag. An additional dashed line where trim drag is approximately zero is shown. As can be expected, it is immediately obvious that both speed of both motors affects the performance of the propeller. When the speed of the first stage motor and, thus, c_{y21} increase the required speed of the second stage motor to produce any thrust is reduced, i.e. the second stage does not have to spin as fast as the first stage to be able to produce thrust. Hence, the dashed line in Fig. 16b, which indicates trimmed operation, curves to the right.

When trim drag is considered, the efficiency is lower except for the region around the line of zero trim drag. It appears that the area where trim drag is sufficiently low that the power efficiency is hardly affected is quite wide.

Figure 17 compares the maximum efficiency at every speed of the first stage motor to the efficiency of the trimmed and the untrimmed SRC from Fig. 11. Peak overall efficiency is slightly above that of the untrimmed SRC implying that there is some recovery of the angular momentum by the second stage. The difference is larger either side of the peak, indicating an increase in angular momentum recovery and resulting in a flatter performance curve for the DRC. Compared to the trimmed SRC, the advantage

0.1

0.05

0

-0.05

┘ -0.1 8 Stator Thrust

Normalised

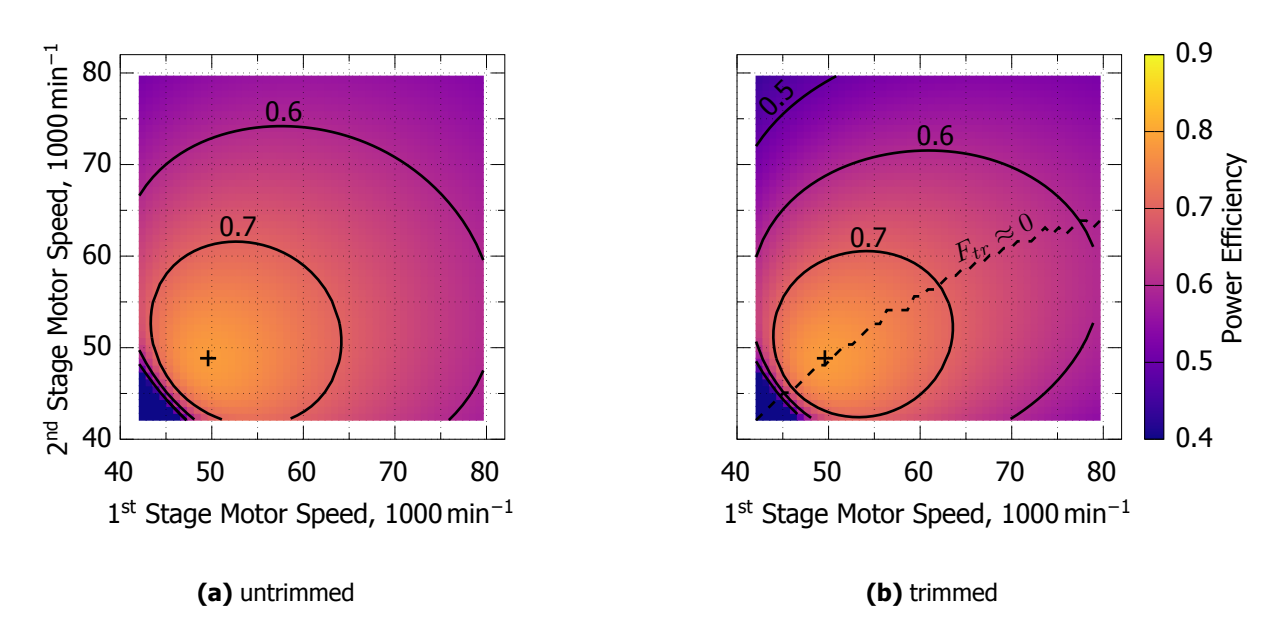


Fig 16. Untrimmed and trimmed power efficiency of a DRC.

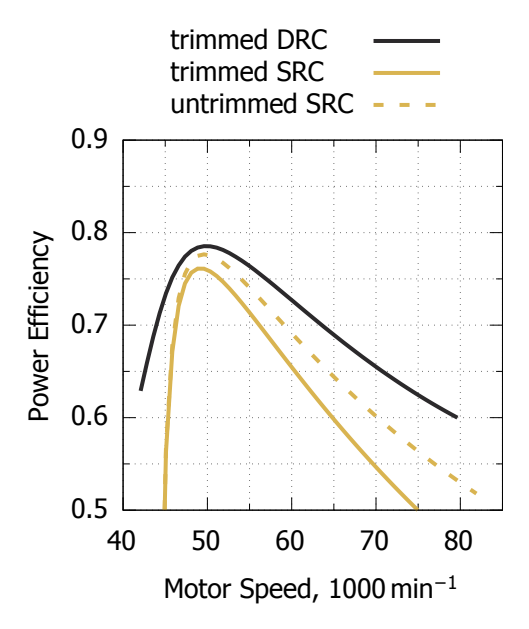


Fig 17. The power efficiency of the trimmed and untrimmed SRC compared to that of the maximum efficiency at any motor speed of the first stage of the complete DRC.

of the DRC is obvious at any rotational speed. The untrimmed DRC is not shown because trim drag is so low for the curve shown that the trimmed and the untrimmed version are almost identical.

There is a clear benefit to using two rotating stages under the assumptions made here. The second stage can be operated in such a way that trimming of the vehicle becomes unnecessary and trim drag is approximately zero resulting in the high efficiency over a wide range.

3.4. CFD Analysis

In the following the results of the CFD analysis of both propeller stages are shown. The flowfield is analysed and a comparison to the quasi 3D model is made. The limitations of the quasi 3D model are that it assumes 2D flow in each cross-section, that the inflow is uniform and that the edges of the blade are perfectly sharp. Meaning that there is no accounting for any flow in the radial direction between cross-sections nor for interactions between the high pressure side and the low pressure side of the blade along the tip. The effects of the propeller hub boundary layer, furthermore, can not be estimated with the quasi 3D model. As far as the leading and trailing edge are concerned, it was shown by Kunze and Paull [22] that for a sufficiently small edge radius, the effects on the power efficiency are negligible.

3.4.1. First Stage

The first stage simulations are performed in a steady state mode. At the range of conditions investigated here, i.e. $46\,000$ rotations per minute to $56\,000$ rotations per minute, the angle of attack varies from -1.15° at the lower end to 9.34° . It is, thus, expected that there will be no unsteady flow features.

Figure 18 shows the power efficiency and thrust power calculated using CFD in comparison to the quasi 3D model. While there is a clear difference between the two models, the largest gap in efficiency is

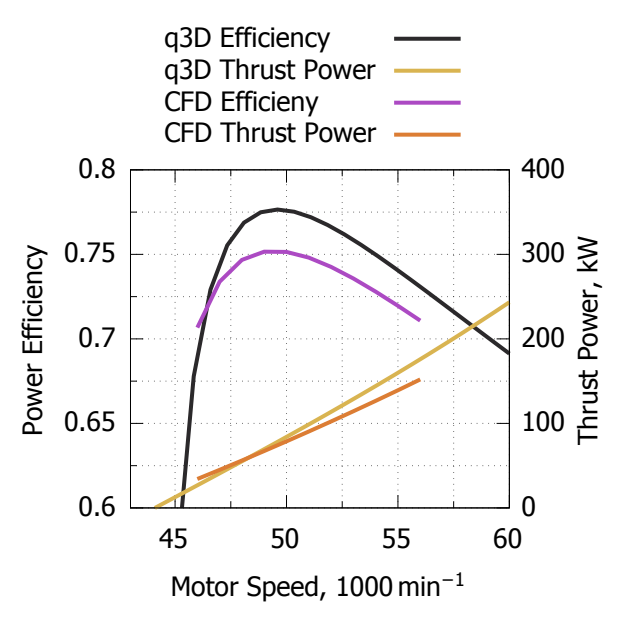


Fig 18. The power efficiency and thrust power over the motor speed of the first stage.

around 2.5 %. Relative to the efficiency calculated using CFD, the quasi 3D model overestimates the performance of the propeller by only 3.3 %. There is also good agreement between the thrust power curves. However, the thrust power curves diverge for increasing motor speeds, which suggests that, despite the better agreement in efficiency, thrust and torque of the propeller are predicted less acurately by the quasi 3D model with increasing motor speeds. The increasing agreement in efficiency is, thus, a consequence of the errors in thrust and torque cancelling out. Nevertheless, considering the limitations of the quasi 3D model, the prediction of propeller performance is very good.

In order to get a better understanding of the differences, the pressure calculated by either model at 50 000 rotations per minute is plotted at three different radii, i.e. 5 mm, 15 mm and 25 mm above the propeller hub, see Fig. 19. The pressures on both the high pressure and the low pressure side are shown in the same plot. In general, the pressures at all three radii agree well. The biggest difference can be seen on the low pressure side at $r=140\,\mathrm{mm}$. This is likely caused by the hub boundary layer. At the centre line of the blade, agreement between the two models is quite good on both sides. Near

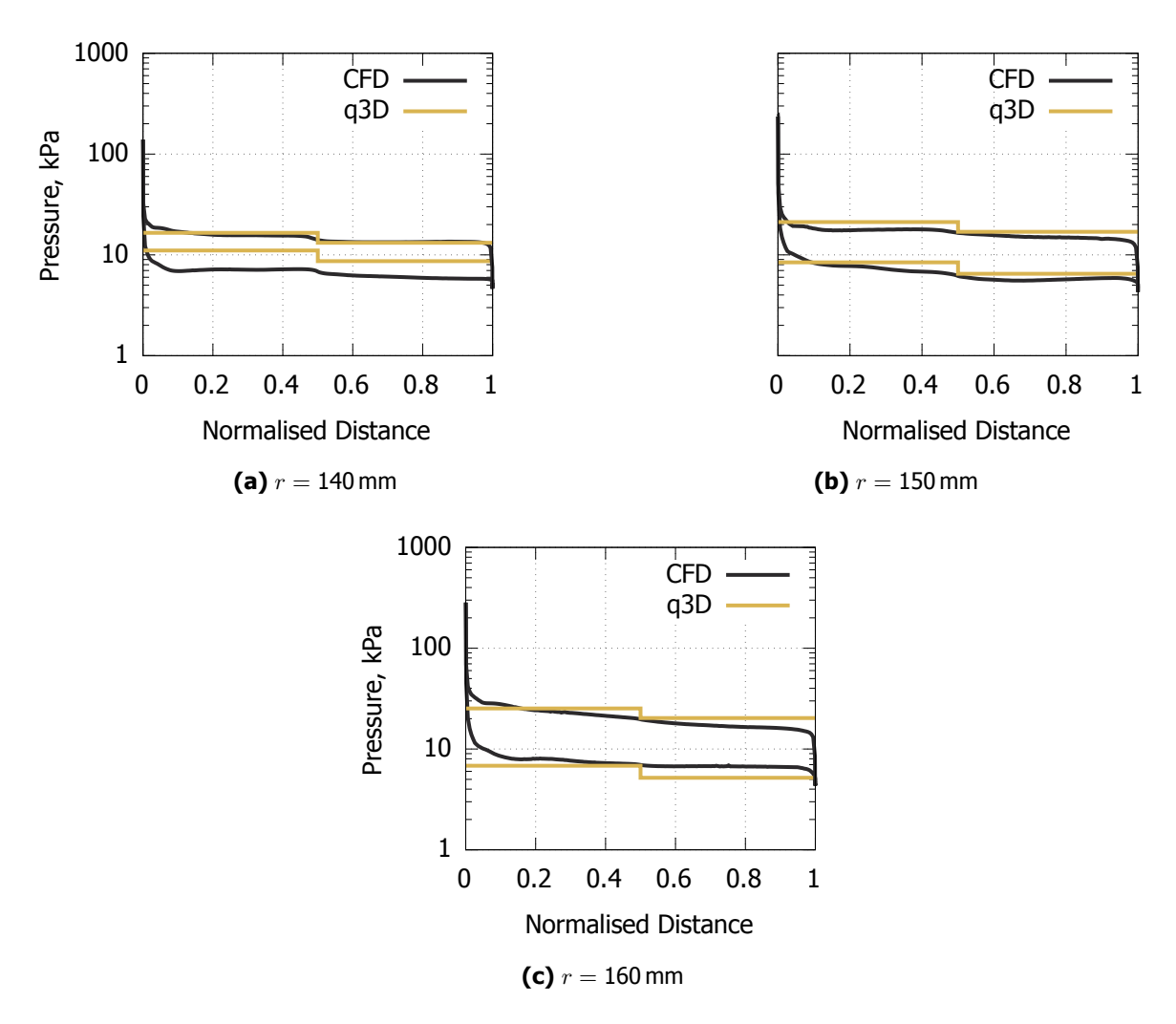


Fig 19. A comparison of the pressure distribution on the first stage between CFD and the quasi 3D model at three different radii.

the tip, i.e. $r=160\,\mathrm{mm}$, the differences are becoming more pronounced again. Here, the quasi 3D model overpredicts the pressure on the high pressure side and underpredicts it on the low pressure side. The CFD curves, furthermore, do not show the pronounced drop in pressure at half the length that the quasi 3D model predicts. These differences can be attributed to interactions of the two sides at the blade tip. At higher motor speeds, where the pressure difference between the two sides becomes more pronounced, tip effects become stronger and likely are the main contributor to the discrepancy between the two models. The inflow profile is independant of motor speed and the hub boundary layer does not change significantly with motor speed either. In summary, the differences between the two models discussed here are primarily attributable to the hub boundary layer and tip effects. Cross-flow and the leading and trailing edge seem to only have minor contributions.

3.4.2. Second Stage

For the simulation of the second stage, the flow properties 6.7 mm downstream of the trailing edge of the first stage are extracted and used as the inflow condition. The simulations themselves are run in an unsteady mode, since the inflow is more complex than it is for the first stage. As discussed in Section 2, the inflow profile here is steady and not rotating as it would be in reality. The velocity vector is transformed between the two stages such that the relative velocities are correct, albeit without the

dependence on time. In order to increase the accuracy of the method, four separate simulations, where the inflow profile is rotated by 15° between any two simulations, were performed. It is postulated, that while unsteady flow phenomena associated with the rotation of the inflow can not be captured with the method used here, the aggregate of the four simulations provides a good approximation of the real flow. Furthermore, major issues, like large flow separations, should be observable with this method. Figure 20 shows the pressure distribution in the inflow plane of all four simulations. It is evident that the wake

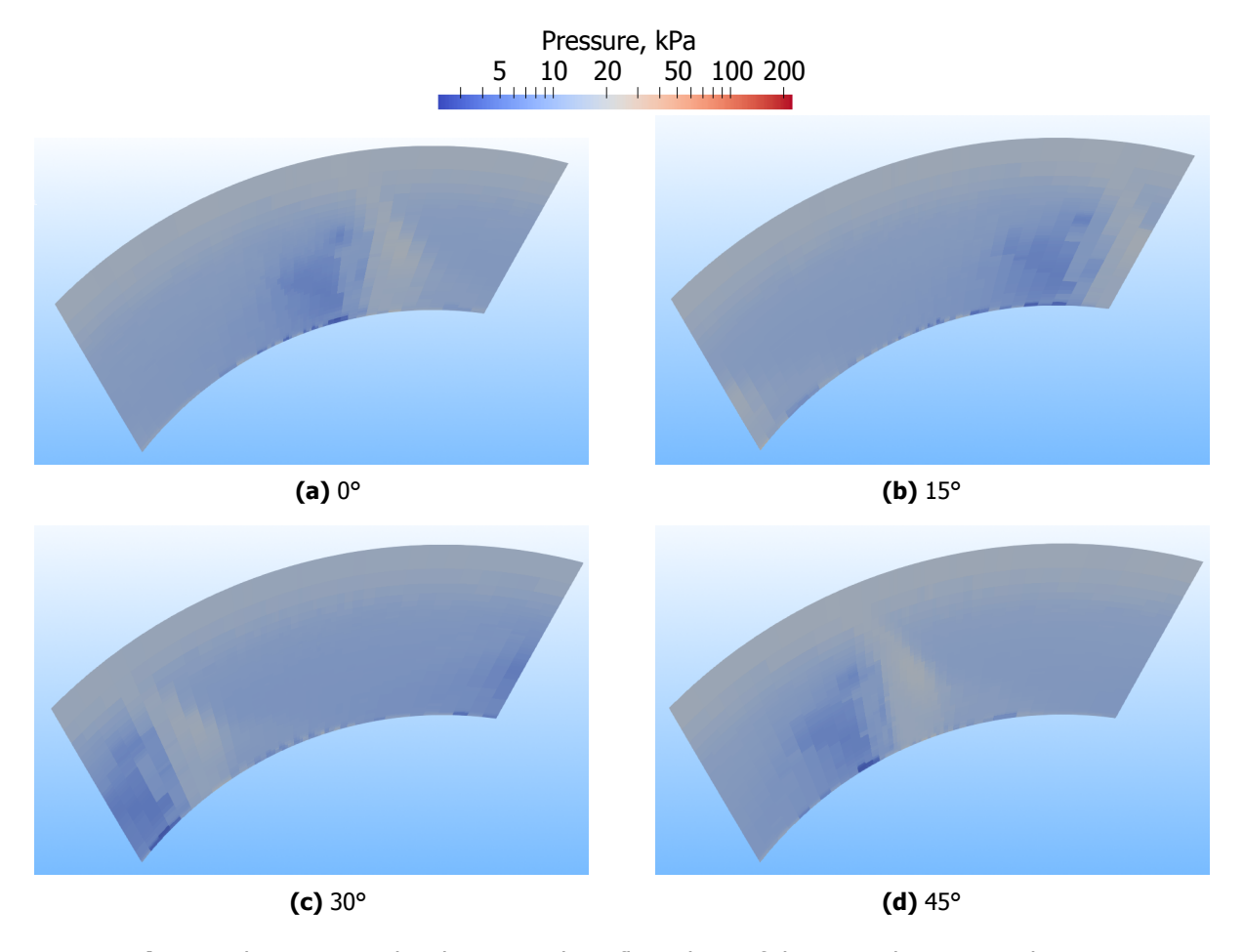


Fig 20. The pressure distribution at the inflow plane of the second stage simulations.

of the first stage, clearly visible just to the right of the centre in Fig. 20a, is in a different location for each simulation.

Figure 21 shows a plot comparing the power efficiency and thrust power of the complete DRC predicted by the quasi 3D model to the aggregate of the four second stage simulations. As for the first stage, the discrepancies in the integrated quantities of the two models are quite small despite the limitations of the quasi 3D model. The quasi 3D model overestimates the power efficiency at $50\,000\,\mathrm{min^{-1}}$ by about 2%, in increase of 2.5% relative to CFD. This is less than the discrepancy for the first stage, although, considering it is a single data point that may be coincidence.

Pressure contours at the same radii as in Fig. 19 are shown in in Fig. 22. The black lines show the mean pressure at each location, the thin grey lines in the background are the pressure contours of the individual simulations. There are considerable differences in pressure on the low pressure side at the smallest radius and on the high pressure side at both other radii between the individual simulations. The mean values, however, agree well with the prediction made by the quasi 3D model. The largest discrepancy, as was the case for the first stage, is on the low pressure side at the smalles radius followed

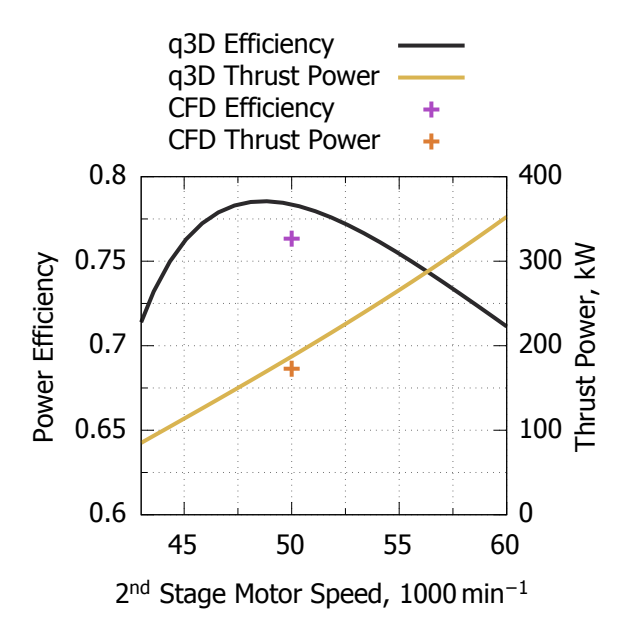


Fig 21. The power efficiency and thrust power over the motor speed of the second stage at $50\,000\,\mathrm{min^{-1}}$ of the first stage.

by the high pressure side closest to the tip. Both of these can, again, be explained by the effects of the hub boundary layer and the tip of the blade. The non-uniformity of the flowfield appears to be less significant.

4. Conclusions

Double-rotor and rotor-stator configurations were analysed and their performance compared to a single-rotor propeller configuration. It was shown that two counter rotating propellers can outperform single-rotor configurations by recovering the angular momentum created by the first stage and eliminating the need for trimming the vehicle about the roll axis. Rotor-stator configurations on the other hand only provide benefits at high motor speed, well past their maximum efficiency. The reason is that the angular momentum behind the first stage at small motor speeds is low and, thus, the viscous drag on the stator outweighs both the reduction in trim drag and its thrust. Best stator performance was found to be at relatively small chord angles, approximately 10 % of the maximum stator angle, for all motor speeds, wich suggests that it is more important for the stator to counter the torque of the first stage and reduce trim drage than to conribute thrust. Finally, a CFD simulation of a DRC was performed and compared to the quasi 3D model. Good agreement was found in general for the first stage and at 50 000 min⁻¹ for the second stage. A single data point, of course, does not allow for a generalised conclusion. However, the good agreement of the pressure contours in particular between the two models is promising. Crucially, CFD predicts no flow features which would prohibit the operation of two counter rotating stages at these conditions, like for instance large flow separations.

While simple models, like the quasi 3D model used here, can not compete with CFD in terms of accuracy and detail, it is often useful to be able to analyse a broad range of conditions and designs in a short amount of time. Compute time alone for the single data point of the DRC using CFD takes several days, whereas DRC performance plots, like Fig. 16 can be generated in a matter of hours with the quasi 3D model. It is, therefore, important to use both methods in a design process, the quasi 3D model for broad performance data and general design features and CFD for validation and detailed design.

For future work, the CFD simulation will be extended to more data points to improve confidence in the conclusions drawn from this study. A higher fidelity model with a rotating inflow condition for the second stage is also in progress. An evaluation of fluid structure interactions as well heating of both the

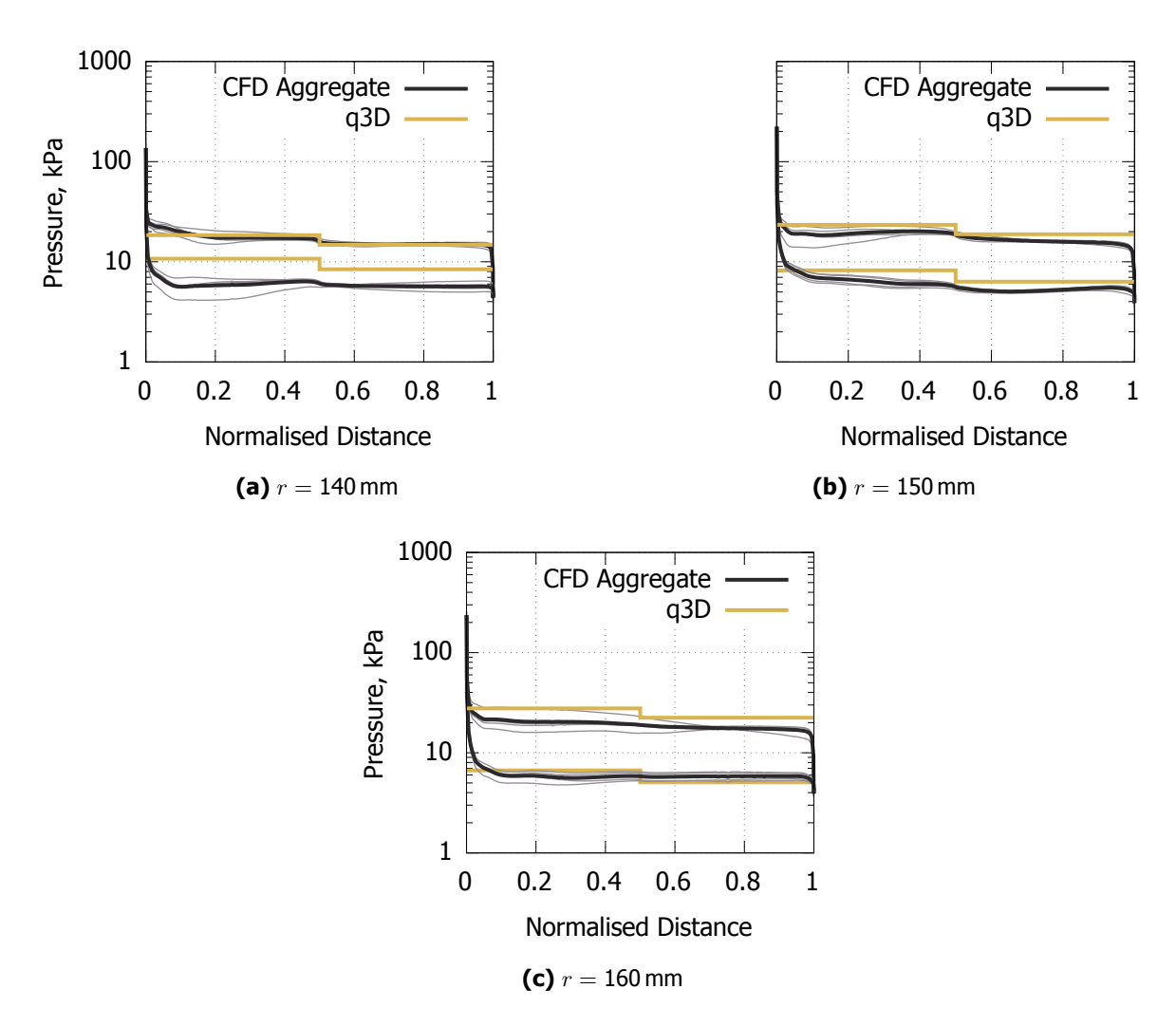


Fig 22. A comparison of the pressure distribution on the second stage between CFD and the quasi 3D model at three different radii.

propeller hub and the blade are also of interest.

Funding

This research was collaboration between the Commonwealth of Australia (represented by the Defence Science and Technology Group) and the University of Queensland, through a Defence Science Partnerships agreement. Further funding was provided by MBDA UK Limited.

References

- [1] H. Budde-Meiwes, J. Drillkens, B. Lunz, J. Muennix, S. Rothgang, J. Kowal, and D. U. Sauer, "A review of current automotive battery technology and future prospects," *Proceedings of the Institution of Mechanical Engineers, Part D: Journal of Automobile Engineering*, vol. 227, pp. 761–776, 5 2013.
- [2] S. Porter, P. Wellener, K. Hardin, and H. Ashton, "Electrification in industrials," 2020.
- [3] S. Paul, "Materials and electrochemistry: Present and future battery," *Journal of Electrochemical Science and Technology*, vol. 7, pp. 115–131, 6 2016.

- [4] D. O'Reilly, G. Herdrich, and D. F. Kavanagh, "Electric propulsion methods for small satellites: A review," *Aerospace*, vol. 8, p. 22, 1 2021.
- [5] S. Darvishpoor, J. Roshanian, A. Raissi, and M. Hassanalian, "Configurations, flight mechanisms, and applications of unmanned aerial systems: A review," *Progress in Aerospace Sciences*, vol. 121, p. 100694, 2 2020.
- [6] X. Liu, D. Zhao, and N. L. Oo, "Comparison studies on aerodynamic performances of a rotating propeller for small-size uavs," *Aerospace Science and Technology*, vol. 133, p. 108148, 2 2023.
- [7] A. Wileman, S. Aslam, and S. Perinpanayagam, "A road map for reliable power electronics for more electric aircraft," *Progress in Aerospace Sciences*, vol. 127, p. 100739, 11 2021.
- [8] S. Xiang, Y. qiang Liu, G. Tong, W. ping Zhao, S. xi Tong, and Y. dong Li, "An improved propeller design method for the electric aircraft," *Aerospace Science and Technology*, vol. 78, pp. 488–493, 7 2018.
- [9] B. J. Brelje and J. R. Martins, "Electric, hybrid, and turboelectric fixed-wing aircraft: A review of concepts, models, and design approaches," *Progress in Aerospace Sciences*, vol. 104, pp. 1–19, 1 2019.
- [10] S. A. Sherrill, P. Banerjee, G. W. Rubloff, and S. B. Lee, "High to ultra-high power electrical energy storage," *Physical Chemistry Chemical Physics*, vol. 13, no. 46, pp. 20714–20723, 2011.
- [11] S. Shelar, "Groundwork for the development of a plasma fuelled engine," 6 2021.
- [12] W. Raza, F. Ali, N. Raza, Y. Luo, K. H. Kim, J. Yang, S. Kumar, A. Mehmood, and E. E. Kwon, "Recent advancements in supercapacitor technology," *Nano Energy*, vol. 52, no. June, pp. 441–473, 2018.
- [13] J. Kunze and A. Paull, "Preliminary analysis of the performance of an electric supersonic propeller," *Aerospace*, vol. 10, no. 9, p. 803, 2023.
- [14] W. C. Strack, G. Knip, J.Godston, and E. Bradley, "Technology and benefits of aircraft counter rotation propellers," NASA, 10 1982.
- [15] A. R. Staff, "Equations, tables and charts for compressible flow," Tech. Rep. NACA Report 1135, Ames Aeronautical Laboritory, 1953.
- [16] W. E. Meador and M. K. Smart, "Reference Enthalpy Method Developed from Solutions of the Boundary-Layer Equations," *AIAA Journal*, vol. 43, pp. 135–139, 1 2005.
- [17] E. H. Hirschel, J. Cousteix, and W. Kordulla, *Three-Dimensional Attached Viscous Flow*. Berlin, Heidelberg: Springer Berlin Heidelberg, 2014.
- [18] B. J. McBride and S. Gordon, "Computer program for calculation of complex chemical equilibrium compositions and applications i. analysis," Tech. Rep. NASA-RP-1311, NASA Lewis Reserach Center Clevelend, OH, 10 1994.
- [19] B. J. McBride and S. Gordon, "Computer program for calculation of complex chemical equilibrium compositions and applications ii. users manual and program description," Tech. Rep. NASA-RP-1311, NASA Lewis Reserach Center Clevelend, OH, 6 1996.
- [20] N. N. Gibbons, K. A. Damm, P. A. Jacobs, and R. J. Gollan, "Eilmer: An open-source multi-physics hypersonic flow solver," *Computer Physics Communications*, vol. 282, p. 108551, 1 2023.
- [21] C. Ventura, E. Sauret, P. Jacobs, P. Petrie-Repar, R. Gollan, and P. V. D. Laan, "Adaption and use of a compressible flow code for turbomachinery design," in *Proceedings of the V European Conference on Computational Fluid Dynamics ECCOMAS CFD* (J. Pereira and A. Sequeira, eds.), pp. 1–3, Portugal: APMTAC/IDMEC, 2010.
- [22] J. Kunze and A. Paull, "Feasibility study of an electric supersonic propeller," in *HiSST: 3rd International Conference on High-Speed Vehicle Science & Technology*, 4 2024.